First-arrival Traveltime Sound Speed Inversion with A Priori Information

Fong Ming Hooi

Paul Carson

Department of Radiology, University of Michigan

Purpose: A first-arrival travel-time sound speed algorithm presented by Tarantola[1] is adapted to the medical ultrasonics setting. Through specification of a covariance matrix for the object model, the algorithm allows for natural inclusion of physical *a priori* information of the object. The algorithm's ability to accurately and robustly reconstruct a complex sound speed distribution is demonstrated on simulation and experimental data using a limited aperture.

Methods: The algorithm is first demonstrated generally in simulation with a numerical breast phantom imaged in different geometries. As this work is motivated by our limited aperture dual sided ultrasound breast imaging system, experimental data is acquired with a Verasonics system with dual, 128 element, linear L7-4 arrays. The transducers are automatically calibrated for usage in the eikonal forward model. *A priori* information such as knowledge of correlated regions within the object is obtained via segmentation of B-mode images generated from synthetic aperture imaging.

Results: As one illustration of the algorithm's facility for inclusion of a priori information, physically-grounded regularization is demonstrated in simulation. The algorithm's practicality is then demonstrated through experimental realization in limited aperture cases. Reconstructions of sound speed distributions of various complexity are improved through inclusion of *a priori* information. The sound speed maps are generally reconstructed with accuracy within a few m/s.

Conclusions: This paper demonstrates the ability to form sound speed images using two opposed commercial linear arrays to mimic ultrasound image acquisition in the compressed mammographic geometry. The ability to create reasonably good speed of sound images in the compressed mammographic geometry allows images to be readily co-registered to tomosynthesis image volumes for breast cancer detection and characterization studies.

I. INTRODUCTION

Speed of sound information when added to B-mode ultrasound images and other modalities improves detection of breast cancer lesions[2–4], with a recent study detecting 100% of the 46 cancer lesions included in the study[5]. Malignant breast cancer lesions have been shown to have an elevated speed of sound of greater than 1500 m/s in comparison to breast fat tissue[6], with some overlap with other breast tissues. Some lipozarcomas, <0.01% incidence, may be rare exceptions[3,7].

Speed of sound imaging of the breast has been pursued in a number of geometries, e.g. ring arrays[2,6] and rotating opposed arrays[3,4]. Several reconstruction algorithms have been devised, from low-order first-arrival flight time[2,6], diffraction tomography methods[8] through higher-order iterative Born approximation[9], and full-wave inverse scattering methods[3]. The main limitations of high order algorithms utilizing the full wave acoustic equation is the ability to characterize the ultrasound transducers to sufficient accuracy in order to properly model the transducers, which remains an active field of research[10–14]. Low order algorithms such as first-arrival methods require only time of flight extraction and minimal data processing, making their practical realization readily possible as illustrated by systems[2,6] in existence presently.

Flight-time algorithms sometimes rely on *ad hoc* tuning of heuristic regularizations and has difficulty producing accurate reconstructions when tomographic angles are limited[15–17]. A more flexible first-arrival flight-time algorithm presented by Tarantola[1] is adapted to the medical ultrasonics setting in this paper. Through specification of a covariance matrix for the object model, the algorithm allows for natural inclusion of physical *a priori* information of the object. The details of the inverse method will be delineated and results will be shown, first using simulated data in various aperture configurations.

As it was motivation for our work, particular emphasis is placed on the algorithm's potential use in limited angle tomography. Specifically, we are studying imaging employing a pair of opposed arrays in our Breast Light and Ultrasound Combined Imaging (BLUCI) system[18]. This device operates in the compressed breast geometry employed in mammography to allow

more accurate comparison of ultrasound and either mammographic or x-ray tomosynthesis images. The various steps necessary to implement the algorithm experimentally is described using an opposed array setup with various sound speed phantoms, including automatic position calibration of the transducers and forward model considerations.

70

This paper serves as a proof on concept as it has only been applied to phantoms and will need additional research for practical use in a clinical setting. Many approaches have been taken to compensate for very limited information available in limited angle tomography[19,20]. However, the improvement in that direction from employing the axial resolution of pulse echo

75 ultrasound holds promise for dramatic, practical improvements in limited angle tomography.

II. METHODS

II.A. Theory

The method's mechanics are briefly described below. The reader is referred to Tarantola[1]

80 for additional background.

The eikonal equation was chosen as the forward model:

$$|\nabla \tau(\vec{x})| = n(\vec{x}) \tag{1}$$

... where τ denotes the *eikonal*, n a propagation time-cost, and $\vec{x}$ a point in the propagation domain. In the acoustic context the time-cost n is the *slowness* (inverse speed) s and the eikonal is the shortest time required to travel from a set sources to a given point within the propagation domain. Validity of the model requires that the characteristic scale of variation

85 of the slowness be much greater than the characteristic wavelength.

The eikonal equation has two primary advantages as a forward model: 1) it may be solved efficiently with multistencil fast marching methods (MSFM); and 2) requires only knowledge of the spatial distribution of sources, allowing the complexity of a complete

90 source characterization to be avoided.

4

An estimate of the slowness contrast profile $\vec{m}$ is obtained via minimization of the cost function:

$$2S(\vec{m}) = \left\|\vec{g}(\vec{m}) - \vec{d}\right\|_D^2 + \left\|\vec{m} - \vec{m}_a\right\|_M^2 \tag{2}$$

...where $\vec{g}$ represents the forward operator which, acting on the slowness (inverse velocity) profile, $\vec{m}$, ($\vec{g}(\vec{m})$) yields predicted flight-time data, $\vec{d}$ represents the measured or simulated flight-time data, and $\vec{m}_a$ is an *a priori* expectation of the profile $\vec{m}$. The weighted norms $\|\cdot\|_D^2$ and $\|\cdot\|_M^2$ are defined:

$$\|\vec{a}\|_D^2 = \vec{a}^t C_D^{-1} \vec{a}, \ \ \|\vec{a}\|_M^2 = \vec{a}^t C_M^{-1} \vec{a}, \tag{3}$$

...where C_D and C_M are the data and profile covariance matrices respectively and $\vec{a}^t$ denotes the transpose of $\vec{a}$. Written explicitly the cost function takes the form:

$$\begin{aligned} 2S(\vec{m}) = & \left(\vec{g}(\vec{m}) - \vec{d}\right)^t C_D^{-1} \left(\vec{g}(\vec{m}) - \vec{d}\right) \\ & + (\vec{m} - \vec{m}_a)^t C_M^{-1} (\vec{m} - \vec{m}_a) \end{aligned} \tag{4}$$

The predicted data $\vec{g}(\vec{m})$ and model parameter $\vec{m}$ can be interpreted as jointly Gaussian random variables with means $\vec{d}$ and $\vec{m}_a$, respectively. Our application deviates slightly from Tarantola as a slowness contrast function is applied for $\vec{m}$ instead, obtained by subtracting background slowness, and $\vec{m}_a$ is set to 0. $\vec{g}(\vec{m})$ will be computed accordingly given the contrast and background slowness.

The cost function is comprised of a weighted data and model space, each with a covariance matrix that allows for inclusion of *a priori* information in the reconstruction. The data covariance matrix (C_D) consists of observed variances of respective flight times (measurement error), while the model covariance matrix (C_M) adjusts for expected sound speed values. Further discussion of the model and data covariance matrices is found in §B2.

The cost function is minimized via nonlinear conjugate gradient updates. The iterations stop when the problem reaches convergence, whose criterion is based on the sum of squared residuals between measured and predicted flight-time data from our forward model for all transmit-receive pairs. For this problem, the stopping criterion is triggered when the fraction of residual error $\frac{|r_n|}{|r_0|}$ reaches a specified tolerance, where r_n is the residual error at the

FIG. 1: Schematic of inverse problem algorithm is shown. The iteration starts with an initial guess using a homogeneous medium, and ends when the problem has converged when the misfit error satisfies a chosen criterion.

nth iteration.

110

High accuracy of the forward eikonal solver and precise knowledge of transmitter and receiver locations to within fractions of a wavelength in a practical setting is essential for convergence. Calibration methods using two commercial transducers mounted in an opposed array geometry will be demonstrated. These methods have been sufficiently accurate 115 to ensure convergence in our inverse problem.

The reconstruction algorithm is summarized below and schematically in Fig. 1. The algorithm is iterative and proceeds through the following series of steps until the convergence criterion is met:

120   1. Compute flight-time map by solving the eikonal equation using current slowness map. Initially, $\vec{m} = \vec{m}_a$, the *a priori* expectation of the model.

   2. Extract flight-time data at receivers and construct a linearized forward model for use in optimization of cost function.

   3. Estimate the slowness contrast by minimizing cost function with appropriate con-
125   straints.

   4. Repeat steps until convergence.

II.B. Application

II.B.1. Eikonal Forward Model

To compute the eikonal equation, a 2D multi-stencil fast marching algorithm is implemented[21,22].
130 Given a source location and a speed map, the model outputs a time-of-flight map from the given source to locations in physical grid space. As receiver location does not always coincide

6

with the chosen grid, bilinear interpolation of four adjacent nodes is performed to extract the flight-time at the receivers.

To compute the path length matrix for the linearized forward model, the path is first traced in physical space following the gradient of the flight-time map from the receiver (which provides a direction vector onto which to traverse) until it reached the source. The path length matrix is then constructed with an appropriate ray thickness to avoid overfitting of the inverse problem on the desired reconstructed grid.

II.B.2. Choice of Covariance Matrices

The primary advantage of the chosen cost function is regularization. The model co-variance matrix (C_M) and *a priori* expectation of the model $(\vec{m}_a)$ allow for inclusion of *a priori* information in the reconstruction: elements of the model $\vec{m}$ may be, e.g., constrained about particular values through appropriate selection of expectation values $(\vec{m}_a)$ and variances (diagonal of C_M) or correlated with other elements through specification of their covariance (C_M). Beyond providing for natural, physically-motivated regularization through specification of *a priori* model variances, when additional *a priori* information is available, significant improvement in image quality can be achieved, especially in limited aperture configurations. Construction of the covariance matrices is examined in detail below.

To construct the covariance matrix, the values are denoted as follows:

$$
C = \begin{pmatrix}
\rho_{11}\sigma_1\sigma_1 & \rho_{12}\sigma_1\sigma_2 & \rho_{13}\sigma_1\sigma_3 & .. \\
\rho_{21}\sigma_2\sigma_1 & \rho_{22}\sigma_2\sigma_2 & \rho_{23}\sigma_2\sigma_3 & .. \\
\rho_{31}\sigma_3\sigma_1 & \rho_{32}\sigma_3\sigma_2 & \rho_{33}\sigma_3\sigma_3 & .. \\
.. & .. & .. & ..
\end{pmatrix}
\tag{5}
$$

where ρ_{ij} is the correlation coefficient between the ith and j^{th} vector element, and σ_i is the standard deviation set for the ith element. Note that the correlation coefficients on the diagonal will always be equal to 1.

A simple 9-pixel image is shown in Fig. 2 to illustrate construction of the covariance matrix. Assuming correlation coefficients of 1 between pixels 4, 7, and 8 and standard

FIG. 2: (Left) Example 9-pixel image to illustrate covariance matrix construction. (Right) A 2D map of the covariance matrix when pixels 4, 7, and 8 are correlated with a coefficient of 1.

deviations of 1 for every pixel, the covariance matrix will resemble a 9 by 9 matrix of:

$$C = \begin{pmatrix} 1 & 0 & 0 & 0 & 0 & 0 & 0 & 0 & 0 \\ 0 & 1 & 0 & 0 & 0 & 0 & 0 & 0 & 0 \\ 0 & 0 & 1 & 0 & 0 & 0 & 0 & 0 & 0 \\ 0 & 0 & 0 & 1 & 0 & 0 & 1 & 1 & 0 \\ 0 & 0 & 0 & 0 & 1 & 0 & 0 & 0 & 0 \\ 0 & 0 & 0 & 0 & 0 & 1 & 0 & 0 & 0 \\ 0 & 0 & 0 & 1 & 0 & 0 & 1 & 1 & 0 \\ 0 & 0 & 0 & 1 & 0 & 0 & 1 & 1 & 0 \\ 0 & 0 & 0 & 0 & 0 & 0 & 0 & 0 & 1 \end{pmatrix} \tag{6}$$

Throughout the paper, selecting probable contiguous regions will be used to improve image reconstructions by applying a correlation coefficient to the proper pixels within the covariance matrix.

The data covariance matrix C_D encompasses experimental noise. As the noise is usually independent from acquisition to acquisition, C_D is comprised of a diagonal matrix with elements of σ, the amount of noise expected from our data acquisition.

The model covariance matrix C_M controls the extent to which the model function varies. Each pixel in the image is treated as a Gaussian random variable with a corresponding mean, $\vec{m}_a$, and standard deviation. Note that if each pixel is deemed independent and allowed to vary identically, C_M is reduced to a constant diagonal and the problem is simplified into Tikhonov regularization. However, since classic Tikhonov algorithms are typically applied in unweighted spaces, the tuning parameter must be frequently optimized to accommodate different experimental setup and reconstruction parameters. Incorporating covariance matrices in weighted spaces eliminates the need for adjusting this tuning parameter, but rather,

allows regularization based on physical expected values for any given experimental setup and domain. Furthermore, C_M enables spatial regularization via correlation coefficients ρ_{ij} between image pixels. In the context of this problem, the variances in C_M were chosen as follows:

$$\sigma = max\left(|s_{minimum} - s_{background}|, |s_{maximum} - s_{background}|\right) \tag{7}$$

Where $s_{background}$ is the slowness of the background, and $s_{minimum}$ and $s_{maximum}$ are the minimum and maximum slowness the model function is expected to attain.

Although the size of the covariance matrices is large (N^2 x N^2), with N being the number of pixels in the image, they are in fact sparse and symmetric. The inverse covariance matrices are estimated using the LSQR method in the context of the equation without direct, prohibitive computation.

II.B.3. Time-of-flight Picker

There are several approaches to time-of-flight extraction, with robust correlation methods given correct windowing[23] and first arrival methods such as the Akaike Information Criterion (AIC)[16] stemming from seismology. A combination of both methods are used to extract time-of-flight information from our experimental data.

An empirical matched filter is first constructed using a water shot dataset for calibration. Using the weighted AIC criterion[16], the window of each receive pulse is extracted by determining the time that the pulse arrives, and as the criterion works symmetrically, the time the pulse finishes as well. The pulses are then averaged to produce a mean receive pulse over all transmit-receive pairs. The transmit pulse in the beginning of each trace is averaged across all traces to obtain an averaged transmit. The mean receive pulse is correlated to this transmit section to obtain the system lag, that is, the delay before the transducer actually begins transmitting pulses. The mean receive pulse is padded with the measured offset to generate the empirical matched filter.

To extract time-of-flight information from experimental data, the first break in the signal is first detected using the AIC picker. A correlation based method with interpolated

RF traces is then implemented using a tight window centered at the detected AIC break. This approach yields a time-of-flight matrix with excellent accuracy when tested with the watershot dataset, with average error ranging from 0.02-0.05 μs, well within the resolution of the sampling rate of the Verasonics ultrasound system.

II.C. Image Reconstruction

II.C.1. Simulations

The algorithm is first demonstrated in a simulated ring aperture configuration. 128 transmitters and receivers are placed in a 6 cm diameter ring with elements equidistant to each adjacent element. Simulated time-of-flight data is obtained via the forward eikonal solver given different speed of sound maps. The imaged object is a numerical breast phantom derived from a breast phantom at Karmanos Cancer Institute, as depicted in Fig. 3, containing a non-uniform skin layer and fat spheres of 1470 m/s, glandular tissue at 1515 m/s, tumor nodules at 1550 m/s, and a background of 1500 m/s. This phantom is scaled slightly smaller than a traditional breast phantom to allow comparison to later linear aperture simulations, and also to facilitate faster computation. The values lie within the $\pm 7\%$ now being reported in breast tissue with a range from 1410 for fat tissue to 1610 m/s for cancers[3]. Random noise with a standard deviation of 0.02 μs is added to the generated time-of-flight dataset.

To begin the iterations, the initial guess for the forward model is set to a homogeneous medium coinciding with the background of 1500 m/s. To aid the inversion, the covariance matrix is constructed to include *a priori* information on expected sound speed values and data measurement error. Since sound speed values in breast tissue reside in the 1400-1600 m/s regime, we set the bounds and compute σ_m accordingly via Eq. 7.

σ_d is set to 0.05 to reflect practical data measurement error as found in calibration. A first reconstruction is done solely with this available *a priori* information without additional regularization parameters; we shall refer to this as basic regularization throughout the pa-

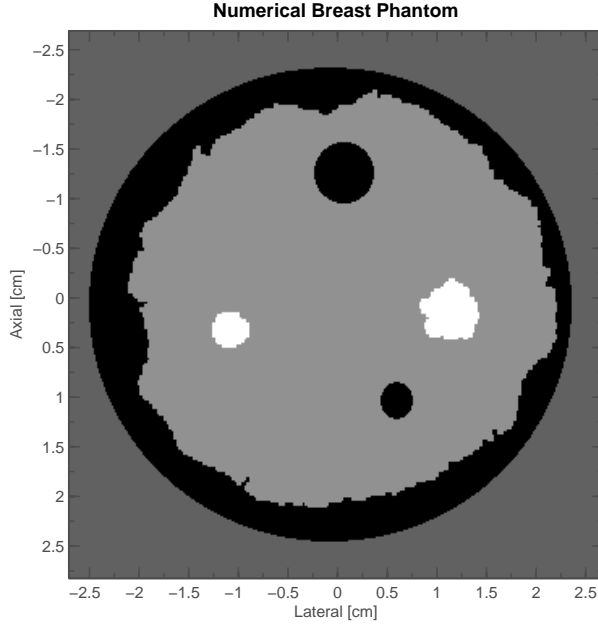**Numerical Breast Phantom**

FIG. 3: (Left) Numerical breast phantom used for simulated reconstructions. The lesions include two high speed tumor nodules, one irregularly shaped, at 1550 m/s, and two fat nodules at 1470 m/s. An irregular skin layer surrounds the phantom with a speed of sound value of 1470 m/s. The entire phantom is placed in a simulated water background of 1500 m/s. (Right) The phantom is manually segmented into contiguous regions to obtain correlated regions for *a priori* information.

per. This regularization is primarily driven by expected values of the model function and independent of reconstruction domain and setup. Correlation coefficients between all pixels are set to 0.

220

To further improve the image, additional *a priori* information can be introduced to the problem such as location of contiguous structure locations and known sound speed regions such as that of homogeneous water background. Manual segmentation of each region is shown in Fig. 3. With this information, the background corresponding to water is constrained to minimal variation by setting the standard deviation of these pixels to a σ_m reflecting 1 m/s variations. The pixels encompassing homogeneous regions are correlated, that is, the correlation coefficient ρ_{ij} were set to a non-zero value of 0.003 when the ith and j^{th} pixels are within a region considered homogeneous. Image reconstruction using data

11

acquired with a ring aperture with basic and additional *a priori* information are depicted in Fig. 6.

The effect of noise on the proposed reconstruction method is examined to demonstrate the robustness of the algorithm. Two primary sources of noise are tested: noise in time-of-flight measurements and location of transmit and receive elements. Images are reconstructed using time-of-flight measurements injected with a Gaussian noise distribution with a standard deviation of 0.1 μs, corresponding to approximately half a waveform cycle operating at 5 MHz. Noise is also introduced in transducer location by varying element locations with a deviation of 0.1 mm from its actual location, corresponding to a $\lambda/3$ discrepancy. The resulting reconstructions are shown in Fig. 7.

As our data acquisition setup in the BLUCI system uses a limited aperture, the rest of the paper will focus on investigating the algorithm in a limited aperture geometry. The same phantom is imaged in this geometry to demonstrate the smearing artifact highly ubiquitous in such acquisitions. To simulate two linear array transducers, 128 transmitters and receivers are placed on opposite sides at a distance of 6 cm at a spacing of 300 μm. The reconstruction with basic and additional *a priori* regularization are demonstrated in Fig. 8. As the choice of correlation coefficient affects the improvement of the reconstruction, using different correlation values is investigated in Fig. 9 using this limited aperture.

II.C.2. Experiments

Two ATL L7-4 linear arrays (ATL/Phillips, Bothell, WA) are mounted opposing each other in a water tank. These probes are connected to the Verasonics ultrasound system which allow for independent channel and element control for speed of sound data acquisitions (Fig. 4). The arrays are comprised of 128, 300 μm elements, which at a distance of 5-6 cm provided approximately an angular range of 30°. The exact locations of the transducer elements are determined via careful water-shot calibration.

Data is acquired at a frequency of 3.75 MHz. Although the frequency is slightly below the bandwidth of the transducer, the pulses look well-formed without signal-to-noise ra-

FIG. 4: Experimental setup with two L7-4 linear arrays. The distance between both transducers was approximately 5 cm apart, which is the average thickness of a compressed breast. A worm rubber contrast is placed in the center and the tank is filled with water for experimental data collection.

(a) Crescent   (b) Dual stranded

FIG. 5: Close up pictures of worm rubber phantoms used.

tio complications. A lower frequency is desirable to ease computation time as the grid is
constructed based on the wavelength. Each element on the transmitter is fired once and recorded on all 128 elements of the receiving transducer for a full RF dataset of 128 x 128 traces.

For each reconstruction, two data acquisitions are obtained: a water shot for system calibration, and an object shot. A 12.5 mm diameter cylindrical phantom made of rubber used for fishing worms (MF Plastics, Ft. Worth, TX) measured to have a speed of sound of 1406 m/s is imaged, along with a crescent shaped and a dual stranded worm rubber phantom separated by approximately 5 mm (Fig. 5).

The reconstruction of the cylinder was initially performed with basic regularization (Fig. 10). Each ray is modeled as a generalized normal distribution where points within the main ray thickness of 300 μm are weighted heavily with a rapid falloff for points located approximately 50 μm beyond the ray thickness specified by a β of 0.7. The ray thickness was chosen to be 300 μm to mirror the element spacing, and is important to prevent over-fitting of the problem solution. The chosen wavelength necessitates a finer grid for proper eikonal computation; thus, adopting a pencil ray (thin line) will result in many untraversed pixels in the image, and consequently, the corresponding pixels may not be updated properly. Distributions specified by various β parameters were examined, but variations showed only minor changes in the image. It is only important that there is slight spatial overlap between adjacent rays to minimize over-fitting.

13

To introduce additional *a priori* information, a grayscale image was obtained using a synthetic aperture focusing technique. Via manual segmentation of this image, local pixels were correlated within the cylinder for an improved reconstruction. The resulting image is shown in Fig. 11.

To investigate the sensitivity of *a priori* information accuracy, the chosen region was intentionally offset in two scenarios: a correlated region was placed largely outside the cylinder to mimic segmenting a non-elevated sound speed region, and a region overlapping both the cylinder and the water background was examined, mimicking an improperly segmented tumor. The reconstructed images resembles that of the reconstruction with basic regularization as depicted in Fig. 12.

The allowed tolerance for deviation of segmented *a priori* regions was further examined, as segmentation may not be very precise in a clinical setting. The correlated region was offset between 0.3 to 6 mm in both the axial and lateral directions, and the corresponding average sound speed was calculated using a circular region with half the diameter of the cylinder in Fig. 13. This smaller region was used to avoid errors due to inclusion of water background pixels near the edge of the cylinder.

As the precise shape of the *a priori* region may be difficult to acquire in patient data, an ellipsoid with different aspect ratios, that is the ratio of the major to the minor axis, was entered as the correlated region to test the effects of shape deviation. Lateral to axial aspect ratios from 0.5 to 2 in increments of 0.1 were examined. The average sound speed was computed similarly to the previous simulation.

Several different phantoms were imaged, including a crescent shaped and dual strand phantom of the same material. For a more complex object, a breast mimicking phantom (Madsen, Madison, WI) with different speed of sound materials ranging from 1412 m/s to 1539 m/s was also examined. Experimental, limited angle transmission data from this phantom with beam aberrating ripples in subcutaneous fat and challenging long lines of high contrast borders nearly bisecting the lesions was reconstructed with the inclusion of *a priori*

information, shown in Fig. 15.

III. RESULTS

III.A. Simulations

In the ring aperture simulations, although slightly noisy, the problem converges and yields the expected speed of sound image with basic regularization in all cases, including those with errors in element location and flight-time in Fig. 7. Regularization with additional *a priori* information provides a more refined image (Fig. 6).

For the linear aperture simulations in Fig. 8, reconstruction with basic regularization yields a very poor image, as expected, due to the limited availability of angles for reconstruction. The discerned lesions are elongated, with the high speed of sound lesions barely visible. The speed of sound values within the distinguishable legions are also not accurate as energy is disseminated along the axial direction. Because a limited aperture is employed in this geometry, elongation and spread ray artifacts similar to those found in other limited angle acquisitions such as in X-ray tomosynthesis were expected. The resolution in the lateral direction is decent but suffers greatly in the axial direction[24].

To improve the reconstructed image using *a priori* knowledge of homogeneous regions, such as that obtainable from pulse echo imaging, the approximate pixels in regions are correlated to further constrain the minimization problem. The resulting image contains highly suppressed artifacts and now resembles the numerical phantom, with speed of sound values deviating a few m/s from the actual value.

The choice of correlation coefficient also affects the improvement of the reconstruction. Reconstructions with different correlation values are demonstrated in Fig. 9 using this limited aperture. Higher correlation coefficients produce a greater improvement in the reconstructed image, although the highest value chosen was only 0.01.
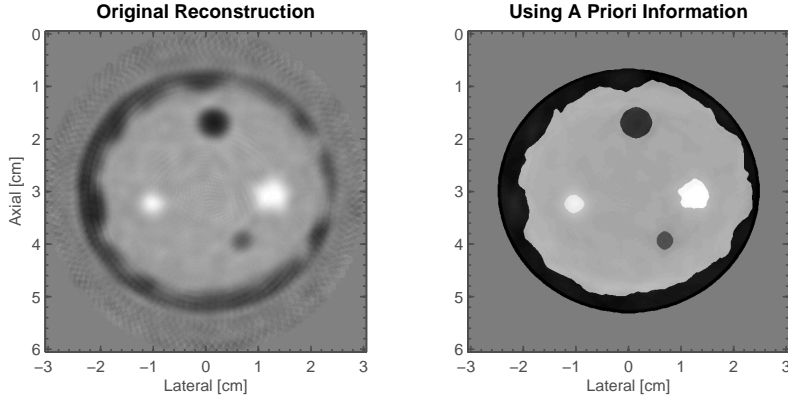
15

FIG. 6: (Left) Reconstructed image of the numerical breast simulation with ring aperture acquisition using regularization based on information on data and model space, including expected speed of sound range and errors in data measurements. The major landmarks of the phantom are reconstructed and discernible in the image. (Right) Reconstructed image with simulated ring aperture acquisition including *a priori* information, utilizing correlation between assumed homogeneous pixels. The resulting image has improved contrast and sharper edges as expected.

III.B. Experiments

When *a priori* information was applied to the algorithm, the reconstructed cylinder showed sound speed values of much better accuracy, with values in the object dipping to approximately 1400 m/s compared to 1440 m/s (Fig. 11). When the region was wrongly segmented, the resulting image shows little improvement over the original image in Fig. 10, with additional artifacts corresponding to the edge of the correlated region within the cylinder (Fig. 12). This result implies that having proper *a priori* information is necessary to facilitate an improved image.

The accuracy of *a priori* information was examined by offsetting the segmented region in both the axial and lateral direction as shown in *Fig.* 13. There is a small tolerance of 1 - 1.5 mm of error in region segmentation in this controlled experimental setup before the reconstructed image starts to degrade towards that of no *a priori* information. When the offset is large, the error in sound speed values in the axial direction becomes larger compared to a similar offset in the lateral direction. The results imply that axial accuracy

16

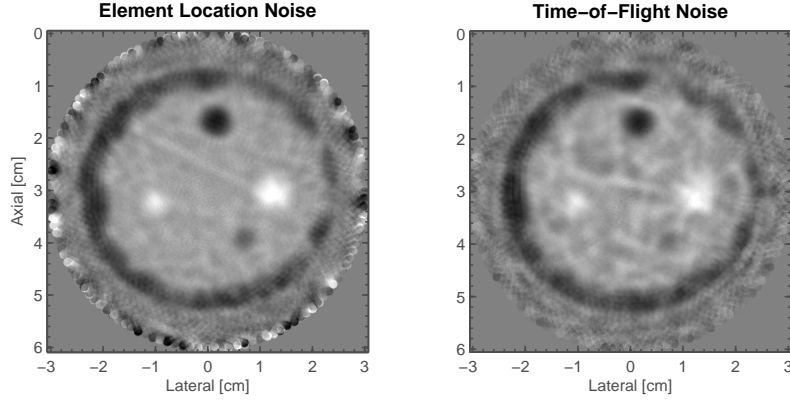**Element Location Noise**   **Time–of–Flight Noise**

FIG. 7: Simulations to examine the effect of noisy measurements on the proposed algorithm. (Left) Reconstructed image of the numerical breast phantom with ring aperture acquisition using noisy time-of-flight data, with a 0.1 μs standard deviation. (Right) Reconstructed image using noisy element location, with a deviation of 0.1 mm.
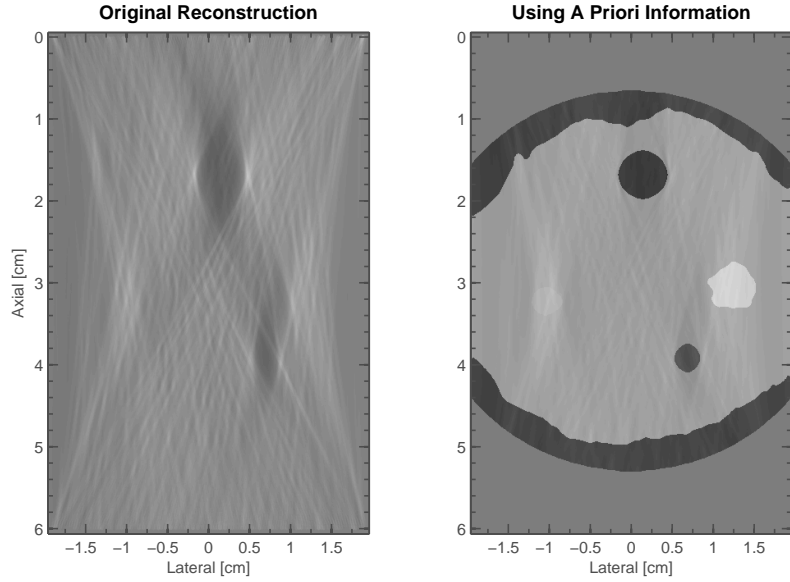

Original Reconstruction   **Using A Priori Information**

FIG. 8: (Left) Image reconstructed using simulated limited aperture acquisition with regularization based on *a priori* information on data and model space. Diamond shaped lesions are noted in the approximate expected locations. Image quality however, is very poor due to limited angle views. (Right) Images reconstructed using simulated limited aperture acquisition with regularization via correlation between assumed homogeneous pixels. The phantom is recovered with suppressed limited aperture artifacts.
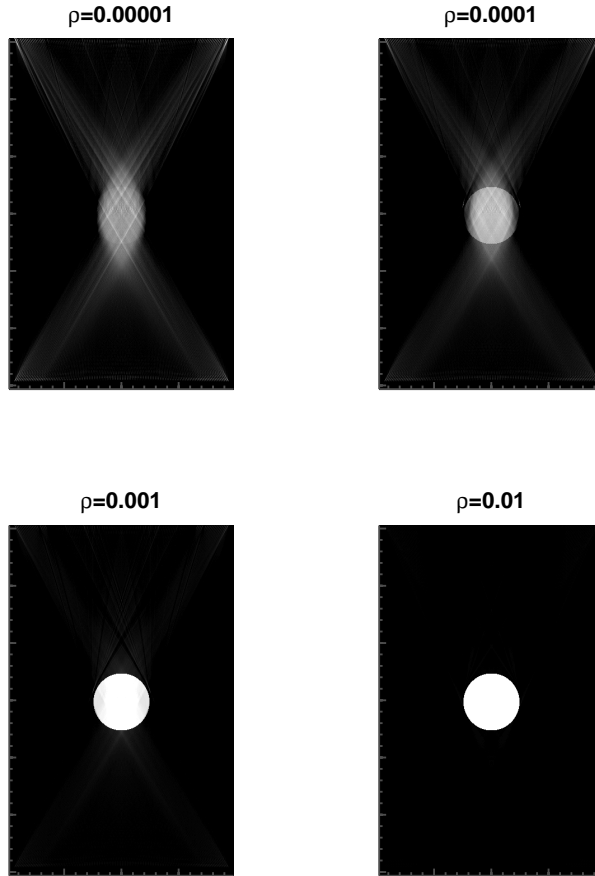
FIG. 9: Images reconstructed from simulation of a single cylindrical object using different correlation coefficient values over the homogeneous region. As the value increased, the smearing artifact due to a limited aperture is diminished. The speed of sound value obtained in the object monotonically approaches the correct value as the correlation coefficient increased.

of the applied *a priori* information can be detrimental if not chosen carefully; fortunately, if extracting information from pulse echo ultrasound, the axial resolution is reasonably good within this tolerance threshold.

The effect of an improper shape was simulated by modifying the correlated region to ellipsoids with different lateral to axial aspect ratios. The errors in sound speed values were much less than those observed when using a wrongly located region, with an average of $<0.5\%$ error. This result suggests that determining the exact boundary is less likely to dramatically skew the sound speed values provided that the region is in the correct location.
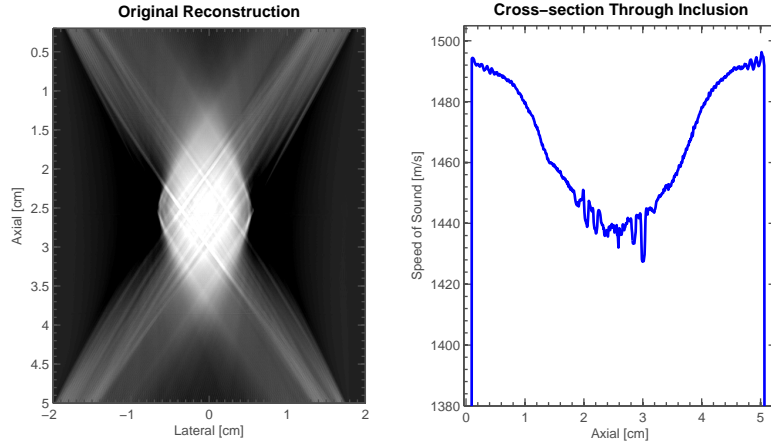
FIG. 10: Experimental data is taken with 128 transmitters and 128 receivers placed in an opposed array geometry with a cylinder of 1406 m/s placed in the center. The object is recovered, and the diamond shaped point spread function is noticeable. The speed of sound within the contrasting cylinder dips to approximately 1440 m/s due to the smearing artifact.

365

Further reconstruction examples were investigated, each introducing *a priori* information extracted from segmenting the accompanying B-mode image. Both the crescent object and the dual strands were recovered with minimal artifacts (Fig. 14). For the breast-mimicking phantom, the calculated speed of sound value for the fat and glandular regions closely

370   matched the actual values, with deviations of a few m/s as shown in Fig. 15. The hypoe-choic lesion exhibited a large speed of sound contrast with values around 1515 m/s relative to the central background of 1457 and fats of high and low speeds of sound on the left and right, respectively, of 1445 and 1415 m/s, which was less than the expected 1539 m/s. This occurred possibly because the lesion resided near the edge of the image, and thus had

375   an even more limited number of angled views in that region and was susceptible to large smearing artifacts. This result demonstrates the importance of positioning the desirable ROI well within the transducer's field of view to minimize the effects of using a limited aperture.
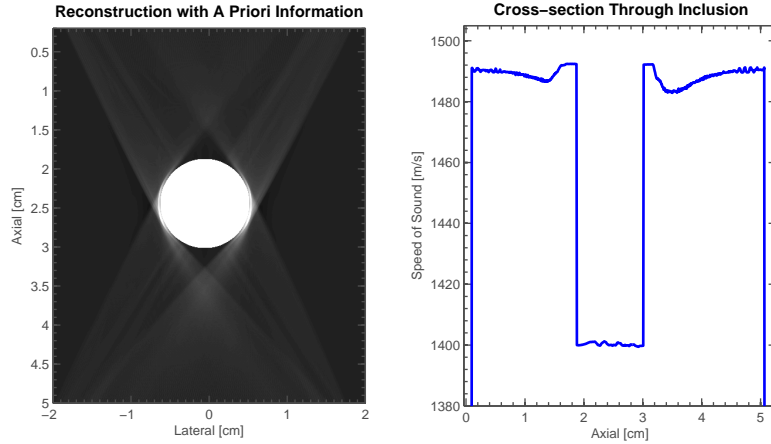
19

FIG. 11: Pixels in the homogeneous region are correlated to aid the inversion of the experimental dataset. The reconstructed speed of sound value reaches approximately 1400 m/s, which is more accurate than the inversion without regularization using correlated pixels.
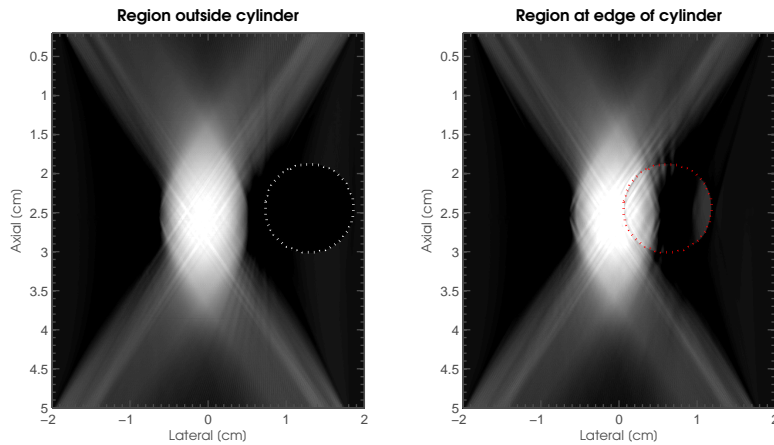

FIG. 12: Pixel correlation of wrongly selected regions, depicted with a dotted outline, show that there is little improvement compared to the original image. When the correlated region encompasses both the cylinder and the background, there are small additional artifacts introduced into the reconstruction.

IV. DISCUSSION

The advantage of this algorithm over other similar algorithms is the ability to define regularization parameters directly based on the physical information of the problem and
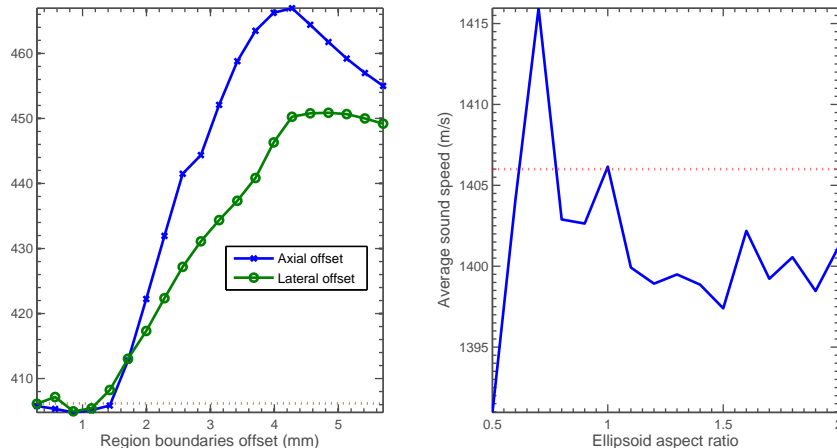
FIG. 13: The segmented region of correlation was offset in the axial and lateral direction between 0.3 and 6 mm to investigate necessary accuracy of *a priori* information to improve image reconstruction. The results suggest an error tolerance within a few mm is still acceptable. Investigating an improper shape for the correlated region by using ellipsoids with different lateral to axial aspect ratios shows that sound speed errors lie typically within 6-7 m/s. The red dotted line represents the true sound speed value of the cylinder.

incorporate spatial *a priori* information. The efficacy of the algorithm is first demonstrated generally in simulation using a traditional numerical breast phantom in two aperture ge-
385 ometries: the common ring aperture, and the opposed array geometry as utilized in our BLUCI system.

Using the ring aperture, the speed of sound image is improved by correlating homogeneous regions within the phantom; the edges are not only sharpened but also the speed of
390 sound values are slightly more accurate in comparison. For instance, the large fat nodule goes from a value of approximately 1461 m/s to 1469 m/s, while the tumor nodule improves from 1549 m/s to 1550 m/s.

While this algorithm is useful generally with various aperture configurations, this algo-
395 rithm is especially useful in improving image quality when tomographic angles are limited. The motivation to explore the algorithm in the dual opposed array geometry was to synergize with our BLUCI system. In the compressed breast geometry, there is no freedom
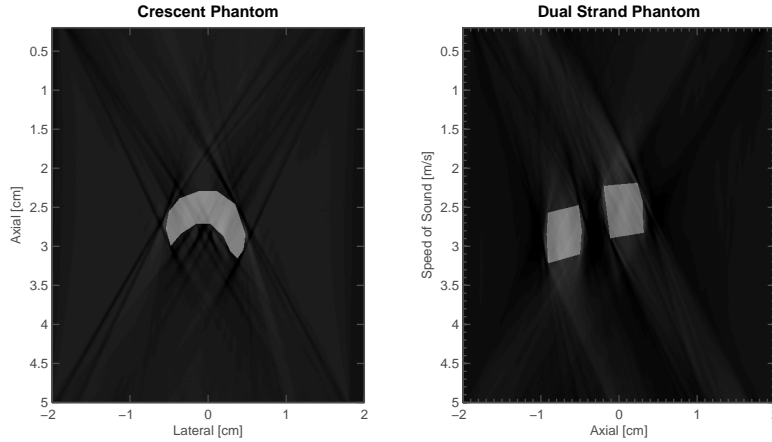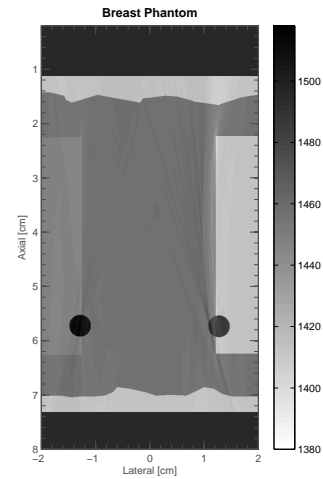
21

FIG. 14: Reconstructed image of crescent shaped and dual strand phantom with *a priori* information using a limited aperture.

(a) Grayscale

(b) Speed of sound

FIG. 15: a) B-mode grayscale image of a breast mimicking phantom. The phantom is comprised of different speed of sound tissue mimicking materials including fat, glandular tissue, and hypoechoic lesions. b) Reconstructed speed of sound map of phantom.

of rotation to obtain angles from the side of the breast. Even if transducers were placed accordingly to acquire the missing angles, the acoustic path length would be quite long, subject to high attenuation and complex beam paths. However, some advantages of the opposed array configuration include traveling through a smaller thickness of the breast, averaging 6 cm instead of approximately 12-15 cm through the coronal breast, allowing use

of a higher central carrier frequency without increased signal attenuation.

405   Various reconstruction algorithms employ total variation (TV) regularization[20,25], which is highly effective in reducing noise while preserving edges. However, with a limited aperture acquisition, the fundamental image includes phantom edges in the axial direction that are inconsistent with the true object, such as that shown in our cylinder reconstruction in Fig. 10. TV regularization by itself would be ineffective given our data acquisition setup, as 410   the total variation of the image "noise" will exacerbate the gradual smearing artifact.

This paper's algorithm avoids using a full wave nonlinear model because such algorithms are difficult to implement due to large computational cost and hardware memory limitations[3,4]. Furthermore, the use of a commercial ultrasound transducer with an eleva- 415   tional focusing lens will have to be characterized[13,14] with high accuracy to obtain a proper forward model. Coupled with the inherent problems of limited tomographic angles, these algorithms may not converge due to the ill-posedness of the problem.

For experimental data, obtaining a precise forward model of the problem is crucial for 420   a working algorithm. As commercial transducer arrays are used, a matching lens layer is placed in the forward solver grid for more accurate results. Setting the values that correspond to the pixels that encompass the entirety of the lens is trivial–at the edges, where the lens does not occupy the complete pixel, a mean sound speed is calculated based on the proportion of the pixel the lens occupied.

425

In order to achieve the level of accuracy necessary for speed of sound reconstructions, grid spacing must be sub-wavelength in size. However, the grid must not be too fine because memory storage and computation complexity increases with $O(N^2)$, with N being the number of pixels. To find the optimal grid cell size, the error found with different cell sizes 430   is compared with analytical truth based on Fermat's principle. Given our linear array setup with focusing lenses, a grid cell size of $\lambda/6$ is ideal to achieve sufficient accuracy. Increasing the precision of the grid past that level depicts little increase in accuracy at a large cost of memory and computation.

An automatic position characterization of the opposed arrays is performed to obtain the locations of each transmit and receive element. Assuming that the transducers do not move once mounted, an inverse problem is solved as follows. The transmit transducer is first set to a fixed location. The algorithm searches for a vector that delineates the location of the receive transducer in terms of axial and lateral distance with respect to the transmit transducer, along with rotation of the transducer where the axis of rotation is perpendicular to the face of the transducer. A minimization problem is solved with an initial crude guess of the axial distance between the transducers and the lateral distance and rotation initialized to 0. In essence, the position of the receiving transmitter is adjusted to minimize the misfit in the cost function defined as the residual sum of squares between computed time-of-flight via the forward model and measured time-of-flight using watershot data.

Note that this minimization problem assumes that the transducers were lined up elevationally because the technique cannot differentiate the difference in time-of-flight when the receiving transducer is in plane with the transmitting transducer, or within the arc of the same distance. The position inversion algorithm is computationally expensive but simply parallel. The inversion is performed by enabling shared memory access within the operating system and taking advantage of a multiple core CPU, readily available within the MATLAB file exchange[26]. This library was also used for parallel computations required in the speed of sound inversion algorithm as well.

The reconstructions were performed on a twelve-core i7 processor machine with each iteration taking approximately three minutes. The number of iterations required for convergence depends on the complexity of the imaged object, with the cylinder taking five iterations and the more complex breast phantom taking approximately sixteen. To speed up reconstructions, future rendition of the code can be ported to languages more suitable for scientific computing such as Fortran or C, and can also take advantage of multi-core GPU processors as well.

The proposed algorithm allows physically-driven regularization of the problem via inclusion of *a priori* information. *A priori* information includes, but is not limited to, knowledge of expected speed of sound values, data measurement error, location of background regions

(water or gel interfaces), and structure information. In a practical setting, this *a priori* information can be obtainable from fat vs. high water content or connective tissue segmentation of pulse echo images of the object, which can be generated from the same RF dataset used to construct speed of sound images. Information from other modalities such as a previous breast or chest MR or CT exam could also be used. Segmentation and registration methods for proper *a priori* information may be investigated for this application in a future study.

With our BLUCI system, current studies include imaging the breast from both sides, photoacoustic tomography of the breast in the same geometry[27], and registration of BLUCI images with combined ultrasound and tomosynthesis images obtained in a different system[28]. The ability to create reasonably good speed of sound images in the compressed mammographic geometry will yield manifold benefits in our system, as they may be more readily co-registered to tomosynthesis image volumes than can pulse echo ultrasound for breast cancer detection and characterization studies. Our work with two sided pulse echo imaging in the lightly compressed breast[18] should allow visualization of the distal side of a breast cancer which is often obscured in a single sided ultrasound image. The same linear arrays employed for pulse echo could be used for this limited angle sound speed imaging.

The *a priori* information regarding the object may be imperfect. Successful reconstruction of the breast mimicking phantom shows promise as it was designed with layers of fat, glandular tissue, and lesions with largely varying sound speeds to produce a distorted ultrasound image. Preliminary investigations in Fig. 12 and 13 show that the output image will not force a value into correlated regions if the observed data does not support a sound speed change within the region; that is, if the wrong location of pixels is correlated or an incorrectly sized region is selected, the object is still approximately reconstructed in the correct location with slight degradation in image quality. Deviation of boundary selection and location of the correlated region showed improved sound speed reconstructions as long as the offset is reasonably small. Starting with segmentation of isolated objects in SOS images may allow centering of corresponding ROIs in the pulse echo images for improved results. A further refined algorithm could also incorporate the correlation region within the cost function and choose the best fit given the initial chosen region.

Since the tested phantoms consist of well-defined contiguous regions, proper segmentations were not difficult to obtain. Additional research will be needed to properly segment more difficult, B-mode breast images into homogeneous regions where shadowing and speckle can degrade edges and contrast. It would also be worthwhile to analyze the algorithm when a only few homogeneous regions can be identified on complex breast tissue.

While additional *a priori* information is not always necessary for convergence as shown in simulation and experiment, the reconstructed image is usually improved when incorporated into the inversion algorithm. As shown in Fig. 9, using stronger correlation coefficients smooths and improves the accuracy of the contrasting cylinder in the reconstructed image. Using a higher correlation coefficient also accelerates convergence, as in the number of iterations needed to obtain the reconstructed image. In our reconstructions, the correlation coefficient was set to be 0.003 since the simulations demonstrated subjectively adequate cleanup of extraneous streaks at this value. Ideally, a very low correlation coefficient should be introduced to guide the inversion towards the correct answer without largely changing the overall cost function. More experience with a variety of phantoms as well as *in vivo* cases will be needed to determine if fixed thresholds will suffice or whether this process can be automated.

The algorithm can be readily generalized to 3D with a high expense in computational complexity. The largest bottleneck with current computer architecture is the limit of available memory to store the L matrices. To transition to 3D, the problem moves from a problem of $O(N^2)$ to $O(N^3)$, with N being the number of reconstructed pixels. Even though our implementation takes advantage of matrix sparsity, only storing the indices and corresponding values of each occupied element, the algorithm still requires a large amount of memory. An optimization that would make a 3D volumetric inversion more practical may be to switch to a coarser grid, thereby lowering the resolution, or to implement a non-uniform grid over regions with little variation.

The inversion algorithm can also be readily extended to simultaneous inversion for attenuation algorithms. It would only require a modification of the cost function and introduction of additional model functions in their respective model spaces.

26

V. CONCLUSION

In this paper, a sound speed reconstruction algorithm allowing inclusion of *a priori* information to improve image reconstruction of phantoms is demonstrated. The ability to form sound speed images using two opposed linear arrays to mimic ultrasound image acquisition in the compressed mammographic geometry is investigated in simulation and experiment. Limited angle tomography is usually plagued by artifacts along the depth of the image when using traditional algorithms. The formulation of this cost function offers elegant regularization driven by physical known values of the problem itself such as the dimensions of high contrast objects and their estimated acoustic properties, which can help improve image quality of limited aperture reconstructions.

A priori information may be garnered from major breast structures noted in ultrasound B-mode, MRI, or X-ray CT images. Depending on the modality, image registration and proper segmentation will be needed to generate usable *a priori* information. The advantage of combining our dual sided ultrasound approach with another modality such as SPECT or DBT (digital breast tomosynthesis) is that breast motion can be constrained, fairly precise borders on both axial sides of a lesion can be delineated with the ultrasound, and the different modality images will already be co-registered as data will be obtained in concurrent patient sessions, though careful calibration will be essential for quality *a priori* information. Even if systems are not combined, the challenging problem of registering ultrasound to mammography or tomosynthesis can be more readily tackled since data is acquired in a similar orientation. The choice of covariance matrices based on this *a priori* information strongly impacts the image quality of limited angle acquisitions. In this separate system approach, current registration algorithms might be adequate for a single, isolated lesion, but probably not for more complex registration over a large region of the breast. Additional investigation on optimal *a priori* information will be necessary for practical application in a clinical setting; determining the optimal covariance matrix to reconstruct *in vivo* images may be investigated thoroughly in a future paper.

ACKNOWLEDGMENT

REFERENCES

[1] A. Tarantola, *Inverse problem theory and methods for model parameter estimation*, siam, 2005.

[2] C. Li, N. Duric, P. Littrup, and L. Huang, "In vivo breast sound-speed imaging with ultrasound tomography," *Ultrasound in Medicine & Biology* **35**, no. 10, 1615–1628, (2009).

[3] M. André, C. Barker, N. Sekhon, J. Wiskin, D. Borup, and K. Callahan, "Pre-clinical experience with full-wave inverse-scattering for breast imaging," in *Acoustical Imaging*, Springer, 2009, 73–80.

[4] J. Wiskin, D. Borup, S. Johnson, M. Berggren, D. Robinson, J. Smith, J. Chen, Y. Parisky, and J. Klock, "Inverse scattering and refraction corrected reflection for breast cancer imaging," in *SPIE Medical Imaging*, International Society for Optics and Photonics, 2010, 76 290K–76 290K.

[5] N. Duric, P. Littrup, C. Li, O. Roy, S. Schmidt, R. Janer, X. Cheng, J. Goll, O. Rama, L. Bey-Knight *et al.*, "Breast ultrasound tomography: bridging the gap to clinical practice," in *SPIE Medical Imaging*, International Society for Optics and Photonics, 2012, 83 200O–83 200O.

[6] C. Li, N. Duric, and L. Huang, "Breast imaging using transmission ultrasound: reconstructing tissue parameters of sound speed and attenuation," in *Biomedical Engineering*

590 *and Informatics, 2008. BMEI 2008. International Conference on*, 2, IEEE, 2008, 708–712.

[7] A. L. Scherzinger, R. A. Belgam, P. L. Carson, C. R. Meyer, J. V. Sutherland, F. L. Bookstein, and T. M. Silver, "Assessment of ultrasonic computed tomography in symptomatic breast patients by discriminant analysis," *Ultrasound in Medicine & Biology* **15**, no. 1, 21–28, (1989).

595 [8] F. Simonetti, L. Huang, and N. Duric, "Transmission and reflection diffraction tomography in breast imaging," in *BioMedical Engineering and Informatics, 2008. BMEI 2008. International Conference on*, 2, IEEE, 2008, 723–727.

[9] M. P. Andre, H. S. Janee, P. J. Martin, G. P. Otto, B. A. Spivey, and D. A. Palmer, "High-speed data acquisition in a diffraction tomography system employing large-scale

600 toroidal arrays," *International Journal of Imaging Systems and Technology* **8**, no. 1, 137–147, (1997).

[10] Y. Kim and P. Nelson, "Optimal regularisation for acoustic source reconstruction by inverse methods," *Journal of Sound and Vibration* **275**, no. 3, 463–487, (2004).

[11] A. Schuhmacher, J. Hald, K. B. Rasmussen, and P. C. Hansen, "Sound source reconstruc-

605 tion using inverse boundary element calculations," *The Journal of the Acoustical Society of America* **113**, 114, (2003).

[12] S.-H. Yoon and P. A. Nelson, "Estimation of acoustic source strength by inverse methods: Part ii, experimental investigation of methods for choosing regularization parameters," *Journal of Sound and Vibration* **233**, no. 4, 665–701, (2000).

610 [13] K. Wang, S. A. Ermilov, R. Su, H.-P. Brecht, A. A. Oraevsky, and M. A. Anastasio, "An imaging model incorporating ultrasonic transducer properties for three-dimensional optoacoustic tomography," *Medical Imaging, IEEE Transactions on* **30**, no. 2, 203–214, (2011).

[14] J. Huijssen and M. D. Verweij, "An iterative method for the computation of nonlinear,

615 wide-angle, pulsed acoustic fields of medical diagnostic transducers," *The Journal of the Acoustical Society of America* **127**, 33, (2010).

[15] Y. Quan and L. Huang, "Sound-speed tomography using first-arrival transmission ultrasound for a ring array," in *Medical Imaging*, International Society for Optics and Photonics, 2007, 651 306–651 306.

620 [16] C. Li, L. Huang, N. Duric, H. Zhang, and C. Rowe, "An improved automatic time-of-flight picker for medical ultrasound tomography," *Ultrasonics* **49**, no. 1, 61–72, (2009).

[17]A. Hormati, I. Jovanović, O. Roy, and M. Vetterli, "Robust ultrasound travel-time tomography using the bent ray model," in *SPIE Medical Imaging*, International Society for Optics and Photonics, 2010, 76 290I–76 290I.

[18]P. L. Carson, F. Zafar, S. A. Verweij, M. M. Goodsitt, G. L. LeCarpentier, S. Sinha, F. Hooi, M. Roubidoux, and J. B. Fowlkes, "Dual sided automated ultrasound system in the mammographic geometry," in *Ultrasonics Symposium (IUS), 2010 IEEE*, IEEE, Oct. 2011.

[19]M. Rantala, S. Vanska, S. Jarvenpaa, M. Kalke, M. Lassas, J. Moberg, and S. Siltanen, "Wavelet-based reconstruction for limited-angle x-ray tomography," *Medical Imaging, IEEE Transactions on* **25**, no. 2, 210–217, (2006).

[20]X. Lu, Y. Yuan, P. Yan, and X. Li, "A novel alternative algorithm for limited angle tomography," in *Image Processing (ICIP), 2011 18th IEEE International Conference on*, IEEE, 2011, 409–412.

[21]M. S. Hassouna and A. A. Farag, "Multistencils fast marching methods: A highly accurate solution to the eikonal equation on cartesian domains," *Pattern Analysis and Machine Intelligence, IEEE Transactions on* **29**, no. 9, 1563–1574, (2007).

[22]D.-J. Kroon, "Accurate Fast Marching," *MATLAB Central File Exchange*," (2011).

[23]T. Chenevert, D. Bylski, P. Carson, C. Meyer, P. Bland, D. Adler, and R. Schmitt, "Ultrasonic computed tomography of the breast. improvement of image quality by use of cross-correlation time-of-flight and phase-insensitive attenuation measurements." *Radiology* **152**, no. 1, 155–159, (1984).

[24]Y.-H. Hu, B. Zhao, and W. Zhao, "Image artifacts in digital breast tomosynthesis: Investigation of the effects of system geometry and reconstruction parameters using a linear system approach," *Medical physics* **35**, 5242, (2008).

[25]K. W. van Dongen and W. M. Wright, "A full vectorial contrast source inversion scheme for three-dimensional acoustic imaging of both compressibility and density profiles," *The Journal of the Acoustical Society of America* **121**, 1538, (2007).

[26]M. Buehren, "Multicore - Parallel Processing on Multiple Cores," *MATLAB Central File Exchange*," (2011).

[27]Z. Xie, X. Wang, R. F. Morris, F. R. Padilla, G. L. Lecarpentier, and P. L. Carson, "Photoacoustic imaging for deep targets in the breast using a multichannel 2d array transducer," in *SPIE BiOS*, International Society for Optics and Photonics, 2011, 789 907–789 907.

[28]S. P. Sinha, M. A. Roubidoux, M. A. Helvie, A. V. Nees, M. M. Goodsitt, G. L. LeCarpentier, J. B. Fowlkes, C. L. Chalek, and P. L. Carson, "Multi-modality 3d breast imaging with x-ray tomosynthesis and automated ultrasound," in *Engineering in Medicine and Biology Society, 2007. EMBS 2007. 29th Annual International Conference of the IEEE*, IEEE, 2007, 1335–1338.

655